Applied Catalysis B: Environmental 317 (2022) 121694

Contents lists available at ScienceDirect

Applied Catalysis B: Environmental

journal homepage: www.elsevier.com/locate/apcatb

CeO_2 nanosheets with anion-induced oxygen vacancies for promoting photocatalytic toluene mineralization: Toluene adsorption and reactive oxygen species

Xiaoqian Wei [a], Ke Li [a], Xueyang Zhang [b], Qing Tong [c], Jiawei Ji [c], Yandi Cai [a], Bin Gao [d], Weixin Zou [a,*], Lin Dong [a,c,**]

[a] State Key Laboratory of Pollution Control and Resource Reuse, School of the Environment, Nanjing University, Nanjing 210023, PR China
[b] Jiangsu Key Laboratory of Industrial Pollution Control and Resource Reuse, School of Environmental Engineering, Xuzhou University of Technology, Xuzhou 221018, PR China
[c] School of Chemistry and Chemical Engineering, Jiangsu Key Laboratory of Vehicle Emissions Control, Center of Modern Analysis, Nanjing University, Nanjing 210023, PR China
[d] Department of Agricultural and Biological Engineering, University of Florida, Gainesville, FL 32611, United States

ARTICLE INFO

Keywords:
Anion-induced oxygen vacancies
CeO_2 nanosheets
Photocatalytic toluene oxidation
Toluene adsorption
Active oxygen species

ABSTRACT

The deep oxidation of toluene is recognized as a major challenge for photocatalytic oxidation of toluene. Herein, we introduced oxygen vacancies into CeO_2 nanosheets through novel anion-removal of Ce-LDH, with the calcining temperatures of 750, 850, 950 °C. The photocatalytic toluene performance was ordered by CeMO-850 > CeMO-750 > CeMO-950, and CeMO-850 had better activity than P25, common CeO_2, and CeO_2-H_2. Different reaction pathways were founded on CeMO photocatalysts, i.e., on CeMO-950 and CeMO-750, the cresol and hydroquinone intermediates were observed, which hindered toluene adsorption/activation and were hard to deep-mineralization. Whereas, more benzoic acid, open-loop oxygen-containing intermediates were observed on CeMO-850, which were resulted from its oxygen vacancies (Ov), i.e., surface Ov and Ce^{3+} were beneficial for toluene adsorption, B acid sites and active radicals' generation, respectively, and bulk Ov were helpful for oxygen mobility and efficient deep-mineralization. The mechanism of Ov generation and toluene degradation were proposed.

1. Introduction

Indoor volatile organic compounds (VOCs) with low concentration, long release time, as well as low relative humidity released by indoor furniture, decoration building materials, kitchen oil fume, etc. could enter the human body through skin contact, respiratory tract intake, and digestive tract intake, which extremely endanger human health [1–3]. In comparison to other technologies for eliminating VOCs, catalytic oxidation is generally regarded as an efficient destructive method. Among them, thermocatalysis and photothermocatalysis have very fatal disadvantages, namely high cost and low stability [4]. However, photocatalytic oxidation is a promising remediation technology for eliminating indoor VOCs with broad practical application prospects due to its mild conditions, eco-friendly, high efficiency, and few by-products [5,6]. In this research field, the main problems that currently exist are the ring opening difficultly of aromatic VOCs and the ambiguous surface reaction mechanism.

Oxygen vacancies have been verified by numerous studies to effectively amend the photocatalytic efficiency and have incited widespread attention. Actually, the introduction of oxygen vacancies can affect the physicochemical properties of the photocatalytic material such as surface chemical state, local atomic arrangement, electronic structure, optical features, and so on [7,8]. Defect states may be generated below conduction band minimum with the formation of oxygen vacancies, which improve photons absorption capacity due to the narrowing of the band gap [9,10]. Zou et al. demonstrated that oxygen vacancies in the

---

* Corresponding author.
** Corresponding author at: State Key Laboratory of Pollution Control and Resource Reuse, School of the Environment, Nanjing University, Nanjing 210023, PR China.
E-mail addresses: wxzou2016@nju.edu.cn (W. Zou), donglin@nju.edu.cn (L. Dong).

https://doi.org/10.1016/j.apcatb.2022.121694
Received 31 March 2022; Received in revised form 23 June 2022; Accepted 29 June 2022
Available online 2 July 2022
0926-3373/© 2022 Elsevier B.V. All rights reserved.

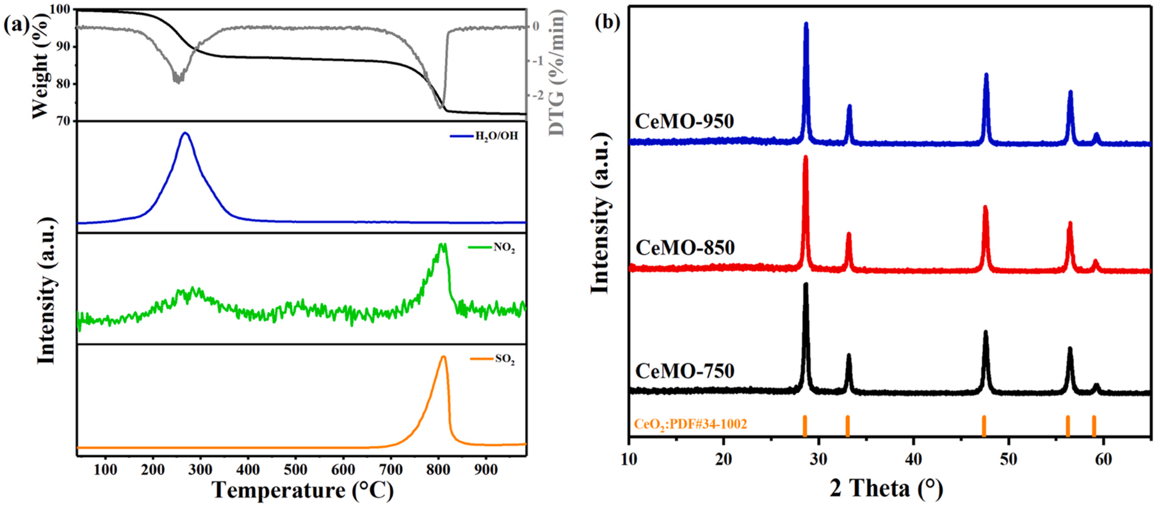

Fig. 1. (a) The TG-MS plots of Ce-LDH. (b) The XRD patterns of CeMO-750, CeMO-850 and CeMO-950 samples.

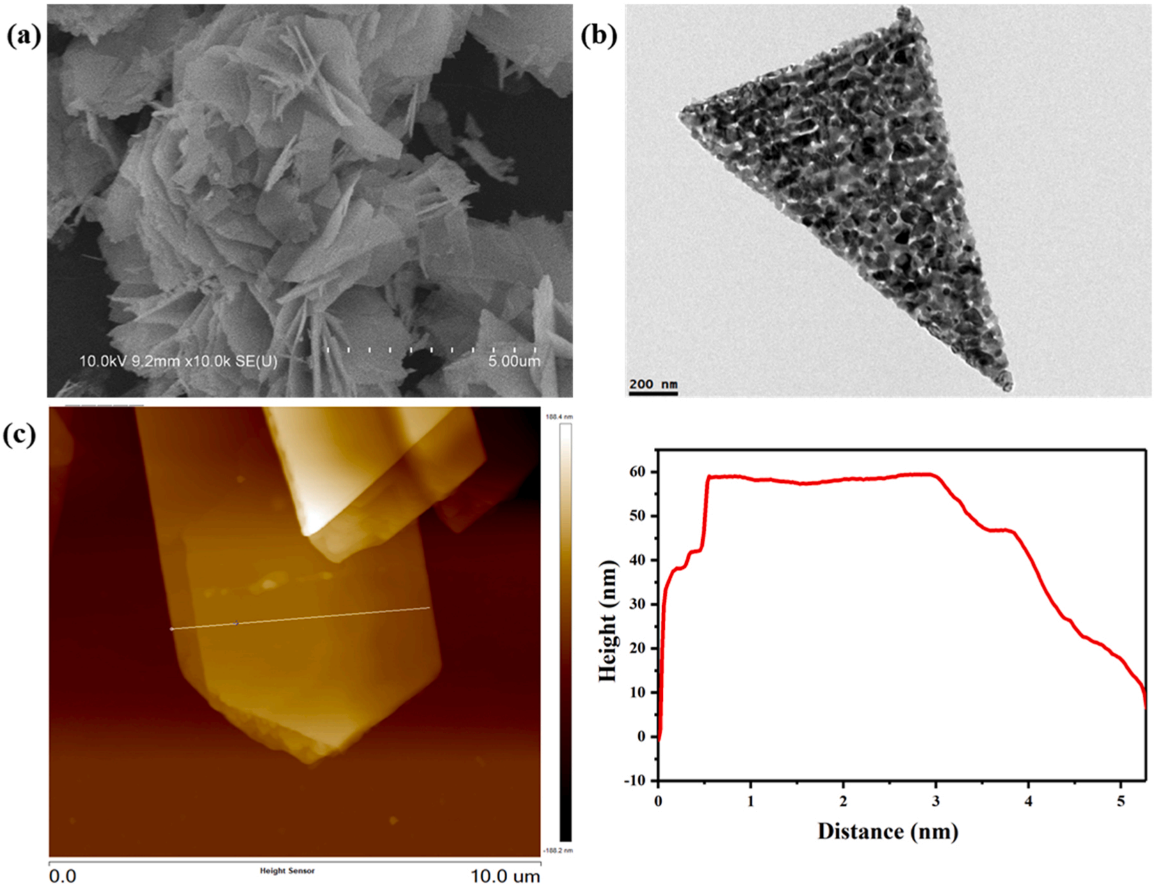

Fig. 2. (a) SEM, (b) TEM and (c) AFM images and the corresponding height profile of as-prepared CeMO-850 sample.

photocatalysts could trap photo-induced electrons to accelerate the separation and transfer of charge carries, thereby facilitating photocatalytic activities of ceria based systems [11]. More importantly, oxygen vacancy defects on photocatalysts surface, the coordinative unsaturated active sites, might help strengthen the adsorption and activation of the reactant molecules, reduce the activation energy barrier, and speed up the surface catalytic reaction [12,13]. Li et al. found that photocatalysts with rich oxygen vacancies tended to activate O_2 molecules into reactive oxygen species (ROS, i.e., $\cdot O_2^-$, H_2O_2, and ·OH) to efficiently oxidize organic pollutants [14]. Similarly, Shen et al. also revealed that the regions containing oxygen vacancies were easier to activate water molecules adsorbed on the surface and generate hydroxyl radicals (·OH) in the photocatalytic process [15]. Interestingly, the oxygen vacancies at the different positions play the different roles in the catalytic reaction process. The surface oxygen vacancies promote the adsorption of the reactant molecules, which are then activated by bulk oxygen vacancies [16,17].

Cerium dioxide (CeO_2), one of the most abundant and functional rare

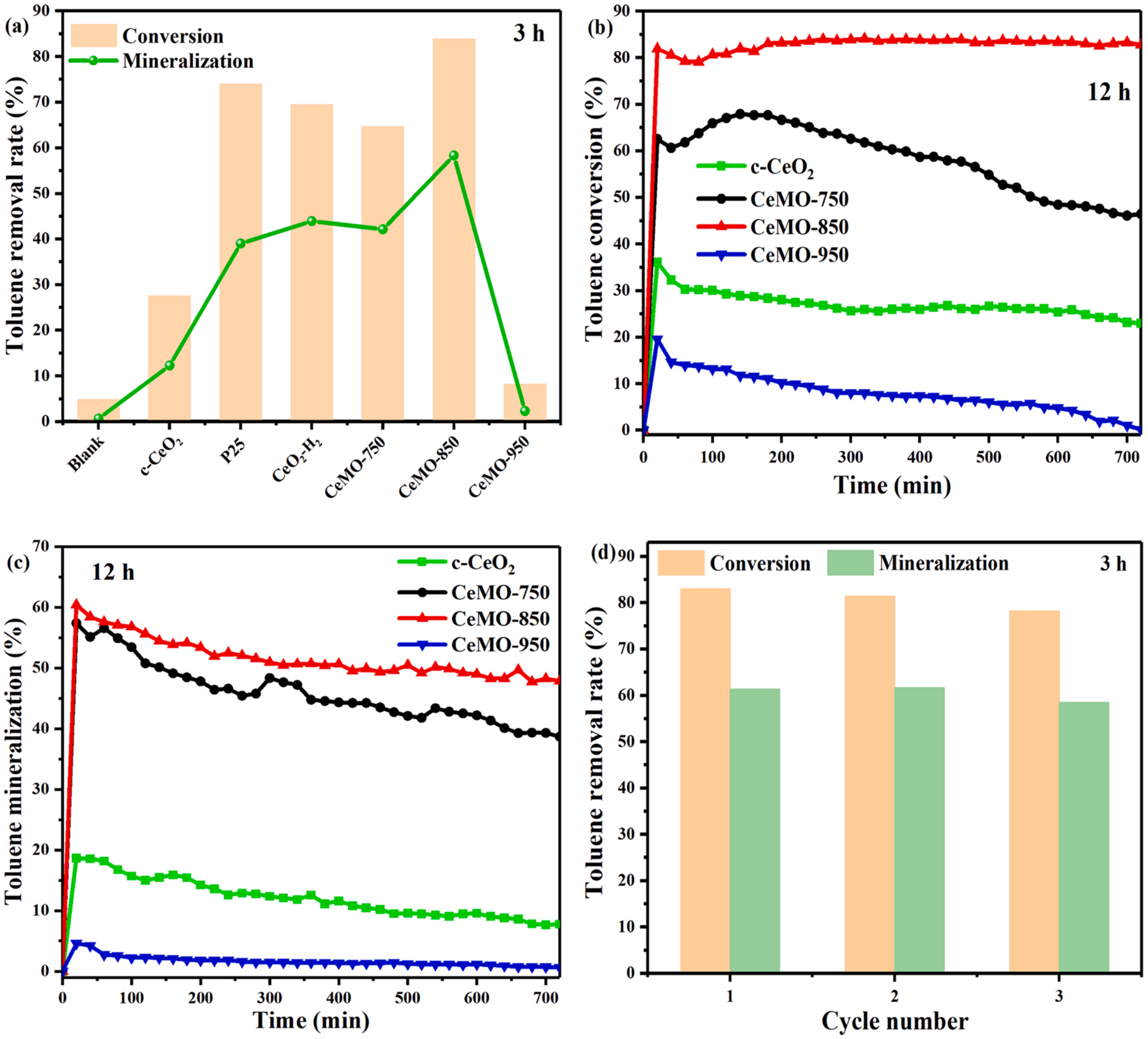

Fig. 3. Removal rate for 3 h (a) and conversion (b) and mineralization (c) for 12 h of toluene by the prepared photocatalysts under light irradiation. (d) reusability of CeMO-850 sample.

earth oxide semiconductors, is a recognized ideal photocatalyst due to the unique 4 f electron transition, the moderate band gap (Eg=2.92 eV), anti-photoirradiation and the large oxygen storage capacity [18,19]. Moreover, a certain amount of surface oxygen defects and circulating Ce^{3+}/Ce^{4+} redox electricity pairs in CeO_2 crystal providing a flowing electronic environment for the photocatalytic reaction system are conducive to activate the reactants, which play a crucial role in photocatalysis [20,21]. Recent research widely showed that introducing more oxygen vacancy defects in CeO_2 could significantly improve its overall photocatalytic performance. Zhang et al. prepared CeO_2 nanorods with different concentration of oxygen vacancies for photocatalytic water oxidation [22]. Both experimental and density functional theory (DFT) calculation results demonstrated that along with the increase of oxygen vacancies, CeO_2 nanorods manifested enhanced optical absorption, charge separation efficiency, and the O_2 generation kinetics. Therefore, the improvement of oxygen vacancies is highly vital in widening the application fields of the CeO_2 phase. Until now, various approaches have been proposed for creating oxygen vacancies in the photocatalysts. Kong et al. achieved ordered porous CeO_2 catalyst with rich oxygen vacancies via redox and steam thermal treatment, which exhibited optimal photothermocatalytic degradation efficiency to VOCs [23]. Chemical reductants are commonly utilized to construct oxygen vacancies. Yu et al. reported on a mineralizer-assisted soft-chemical method to successfully introduce oxygen vacancies on the $Sr_2Bi_2Nb_2TiO_{12}$ surface in situ, displaying superior CO_2 photoreduction activity [24]. In addition, ion doping is also a typical method for oxygen defects implantation. Xu et al. successfully synthesized defected ZnO crystal through Ni doping induced means and noticed that proper concentration of surface oxygen vacancies could get optimum photocatalytic activity [25]. However, these methods may make the formed defects uneven. And there are few studies on the in situ generation of oxygen vacancies by anion-induced to improve photocatalytic activity of toluene.

Layered double hydroxide (LDH), an important class of two-dimensional layered nano-sized materials, is comprised of an edge-sharing MO_6 octahedron host layers with the metal cations occupying the center and embedded interlayer anions and water molecules [26,27]. Recently, it has been reported that the calcined LDH (MMO) would be a new type of photocatalytic material system with potential applications [28]. Ye et al. heat-treated monometallic cerium layered double hydroxides increasing concentration ratio of Ce^{3+}/Ce^{4+} and surface area, showing perfect photocatalytic activity towards photoreduction of CO_2 [29]. Chen and coworkers successfully synthesized Ag_3PO_4/-calcined Zn-Al layered double hydroxides heterostructure photocatalyst with improved photocatalytic activity for TC degradation [30]. During the LDH heat treatment process, due to the removal of water molecules and the decomposition of interlayer anions, the MMO with certain nanopores and structural defects could be acquired. Compared with other methods of introducing oxygen vacancies, this anion-induced

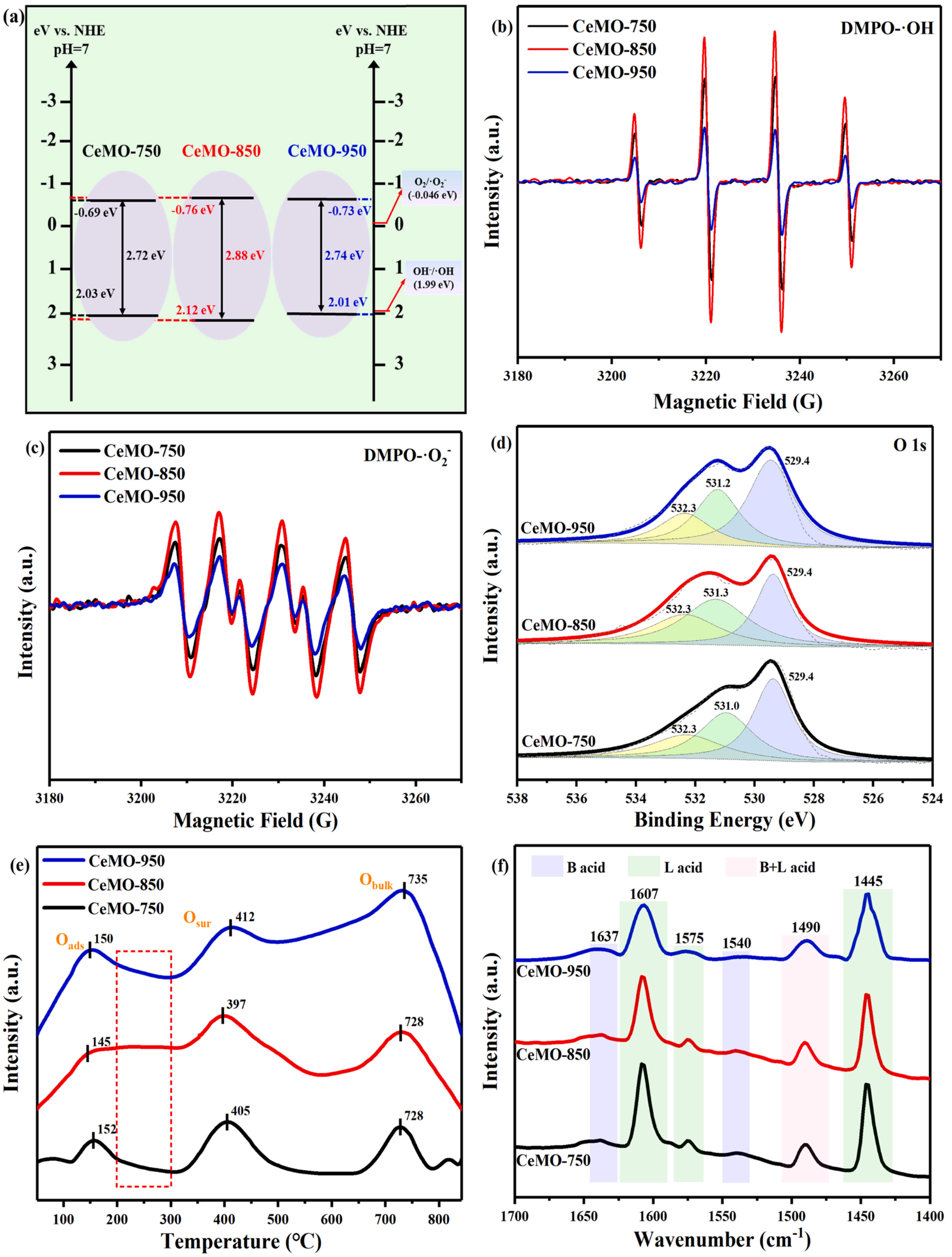

Fig. 4. The band structure (a) and ESR spectra under light irradiation for 10 min for (b) DMPO-·OH and (c) DMPO-·O_2^- of CeMO-750, CeMO-850, and CeMO-950. (d) XPS spectra of O 1s, (e) O_2-TPD, and (f) Py-IR spectra of the calcined Ce-LDH samples.

oxygen vacancy strategy can effectively create uniform oxygen vacancy defects in photocatalysts. In general, the boosting catalytic activity is attributed to the abundant oxygen vacancies of the catalyst. However, little attention has been paid to the roles of surface oxygen vacancies, bulk oxygen vacancies and surface Ce^{3+} species in CeO_2 for photocatalytic oxidation of toluene.

Based on the importance of oxygen vacancy for photocatalytic toluene removal and advantages of anion-induced oxygen vacancy method, we developed an anion-induced oxygen vacancy strategy of calcining Ce-LDH at different temperatures to synthesize CeO_{2-x} photocatalysts with different oxygen vacancies (CeMO). The letter "M" in the sample name "CeMO" stand for the corresponding metal oxides (MO) after calcination of layered double hydroxide (LDH). The obtained CeMO samples were employed for photocatalytic removal of toluene, a

Table 1
Acid amount information obtained from Py-IR spectra of CeMO samples at 40 °C.

Sample	Desorption amount (μmol/g)	
	B acid sites	L acid sites
CeMO-750	3.55	40.22
CeMO-850	4.32	35.75
CeMO-950	2.72	41.23

typical indoor aromatic VOCs with high toxicity. The specific objectives of this work are as follows: (1) the formation mechanism of oxygen vacancies of the anion-induced method, characterize their morphological, physicochemical, and photoelectric properties; (2) evaluate the key factors to photocatalytic activity and stability of as-synthesized CeMO for toluene; (3) measure and calculate the adsorption and activation capacity of toluene by CeMO; (4) unveil the role of surface and bulk oxygen vacancy in the generation of ROS; and (5) clarify the photocatalytic degradation mechanism of toluene. We proposed that the work would provide effective ways to photocatalytic opening loops, mineralization, and removal of toluene.

2. Experimental section

2.1. Synthesis of materials

Deionized (DI) water was used in the whole experiment. Notably, all the reagents used in this work were of analytical grade and had not been further purified. The CeO_{2-x} nanosheets were synthesized according to the method described in the literature [29]. The optimal molar ratio of $(NH_4)_2S_2O_8/Ce(NO_3)_3$ during the Ce-LDH preparation was determined by the effects of $(NH_4)_2S_2O_8$ contents on the forming Ov, and the descriptions of the optimal details were displayed in the supporting information (Section 1). Thus, the optimal molar ratio of $(NH_4)_2S_2O_8/Ce(NO_3)_3$ at 0.6 was selected in our work. Typically, 0.4342 g of $Ce(NO_3)_3.6\ H_2O$, 0.7597 g of NaCl, 0.7010 g of hexamethylenetetramine ($C_6H_{12}N_4$) and 0.1369 g of $(NH_4)_2S_2O_8$ were added into the flat-bottomed flask within 200 mL of DI water, and magnetically stirred to obtain a clear mixed solution. The solution was refluxed at 110 °C for 24 h under the protection of high purity argon. After being cooled naturally to room temperature, the resulting suspension was centrifuged and washed with ethanol and DI water for several times, then vacuum dried for 24 h at 60 °C and obtained the Ce-LDH material. Afterward, it was calcined at 750 °C, 850 °C and 950 °C for 6 h with a heating rate of 5 °C/min in a muffle furnace. The corresponding samples were denoted as CeMO-750, CeMO-850 and CeMO-950, respectively. For comparison, $Ce(NO_3)_3.6\ H_2O$ was directly calcined at 850 °C for 6 h with a heating rate of 5 °C/min in a muffle furnace, which got common CeO_2 and was labeled as c-CeO_2. Besides, to illustrate the advantages of the anion-induced oxygen vacancies method, CeO_2 was prepared by traditional H_2 post-treatment means. $Ce(NO_3)_3.6H_2O$ was calcined at 550 °C for 4 h in a muffle furnace, then kept for 4 h at 450 in a tube furnace under H_2, which was marked as CeO_2-H_2.

2.2. Characterization of materials

X-ray powder diffraction (XRD) analysis of the photocatalysts was carried out using a Philips X′Pert Pro diffractometer with Ni-filtered Cu Kα radiation. The scanning electron microscopy (SEM) was obtained from an SSX-550 instrument. Transmission electron microscopy (TEM) and high-resolution TEM (HRTEM) were conducted on a JEM-2100 instrument at an acceleration voltage of 200 kV. Atomic force microscope (AFM) was taken on Bruker Dimension Edge. Specific surface area and pore structure of the samples were tested on the Micrometrics ASAP-2020 instrument. X-ray photoelectron spectroscopy (XPS) spectra were collected on a PHI 5000 Versa Probe spectrometer and calibrated using the carbonaceous C 1 s line at 284.6 eV. X-Ray Fluorescence (XRF) test was performed on a Bruker M4 Tornado with 20 m spot size and a rhodium anode tube operated at 50 kV, 600 A, no filter and dual Bruker XFlash Series 6 detectors, in vacuum. Thermogravimetry and differential thermal analysis (TG-DTA) was performed on a STA 449 C device from 20 °C to 900 °C with a ramping rate of 20 °C/min in a stream of air. Fourier transform infrared (FT-IR) spectra were recorded on a NICOLET iS10 FT-IR spectrometer. In situ UV Raman spectra were collected from 50 °C to 600 °C with 50 °C intervals. Laser Confocal Raman spectra were acquired from a LabRAM Aramis instrument equipped with an He-Cd laser beam with an emission line at 325 nm. H_2-temperature programed reduction (H_2-TPR) was tested from 50 °C to 900 °C in a flowing 7% H_2/Ar stream. Before the measurement, the sample was pretreated at 400 °C for 1.5 h in a purified N_2. The electron spin resonance (ESR) was operated on a JES FA200, JEOL Co. spectrometer. Toluene/O_2-temperature programed desorption (Toluene/O_2-TPD) test were performed on a Chembet Pulsar apparatus (QUANTACHROME) after the sample was pretreated in pure He atmosphere for 1.5 h at 400 °C. The toluene adsorption kinetic (25 °C) and desorption process (25–600 °C) were determined by the TGA experiment (TGA/DSC 3 +, Mettler Toledo). Similarly, the sample was pretreated at 400 °C for 1.5 h under the pure N_2. The pyridine adsorbed IR spectroscopy (Py-IR) was obtained after evacuation for 30 min at 40 °C. The intermediate products of catalyst surface (CeMO-S) and reaction exhaust (CeMO-G) were first absorbed by liquid ethyl acetate for 3 h and further detected by gas chromatography–mass spectrometer (GC-MS, ISQ, Thermo) with pure He as mobile phase. UV–vis diffuse reflectance spectrophotometer (UV-3600) was used to identify optical absorption properties. Photoluminescence (PL) spectra were obtained using a F-7000 fluorescence spectrophotometer with the excitation light of 325 nm wavelength. The transient photocurrent response and electrochemical impedance spectroscopy (EIS) curves were measured on a CHI660E electrochemical workstation using an Ag/AgCl electrode as the reference electrodes and 0.1 M of Na_2SO_4 as electrolyte solution. *In situ* diffuse reflectance infrared Fourier transform spectroscopy (DRIFTS) was collected by a Nicolet Nexus 5700 FTIR spectrometer. Each photocatalyst was primarily pretreated for 1.5 h at 400 °C with purified N_2, and then cooled to 30 °C to collect the sample background spectra. Thereafter, toluene adsorption DRIFTS was recorded for 40 min with the introduction of 20 ppm toluene/air. *In situ* DRIFTS of photocatalytic toluene experiments were conducted under the illumination of a Xe lamp in 20 ppm toluene/air atmosphere.

2.3. Computational methodology

We have employed the Vienna Ab Initio Package (VASP) to perform all the density functional theory (DFT) calculations within the generalized gradient approximation (GGA) using the PBE formulation [31–33]. We have chosen the projected augmented wave (PAW) potentials to describe the ionic cores and take valence electrons into account using a plane wave basis set with a kinetic energy cutoff of 450 eV [34,35]. Partial occupancies of the Kohn–Sham orbitals were allowed using the Gaussian smearing method and a width of 0.05 eV. The on-site corrections (DFT+U) has been applied to the 4 f electron of Ce atoms (U_{eff} = 5.0 eV) by the approach from Dudarev et al. [36]. The electronic energy was considered self-consistent when the energy change was smaller than 10^{-5} eV. A geometry optimization was considered convergent when the force change was smaller than 0.02 eV/Å. Grimme's DFT-D3 methodology was used to describe the dispersion interactions [37].

As illustrated in Fig. S3, the CeMO samples possess lattice fringes spacing of 0.32 nm matching well with CeO_2(111) [11]. Meanwhile, the results of XPS, Raman, and ESR indicated the existence of oxygen vacancies in CeMO materials. So, the models of CeO_2(111) with and without oxygen vacancies were used to calculate its adsorption and activation capacity for toluene.

The equilibrium lattice constant of CeO_2 unit cell was optimized, when using a 11 × 11 × 11 Monkhorst-Pack k-point grid for Brillouin

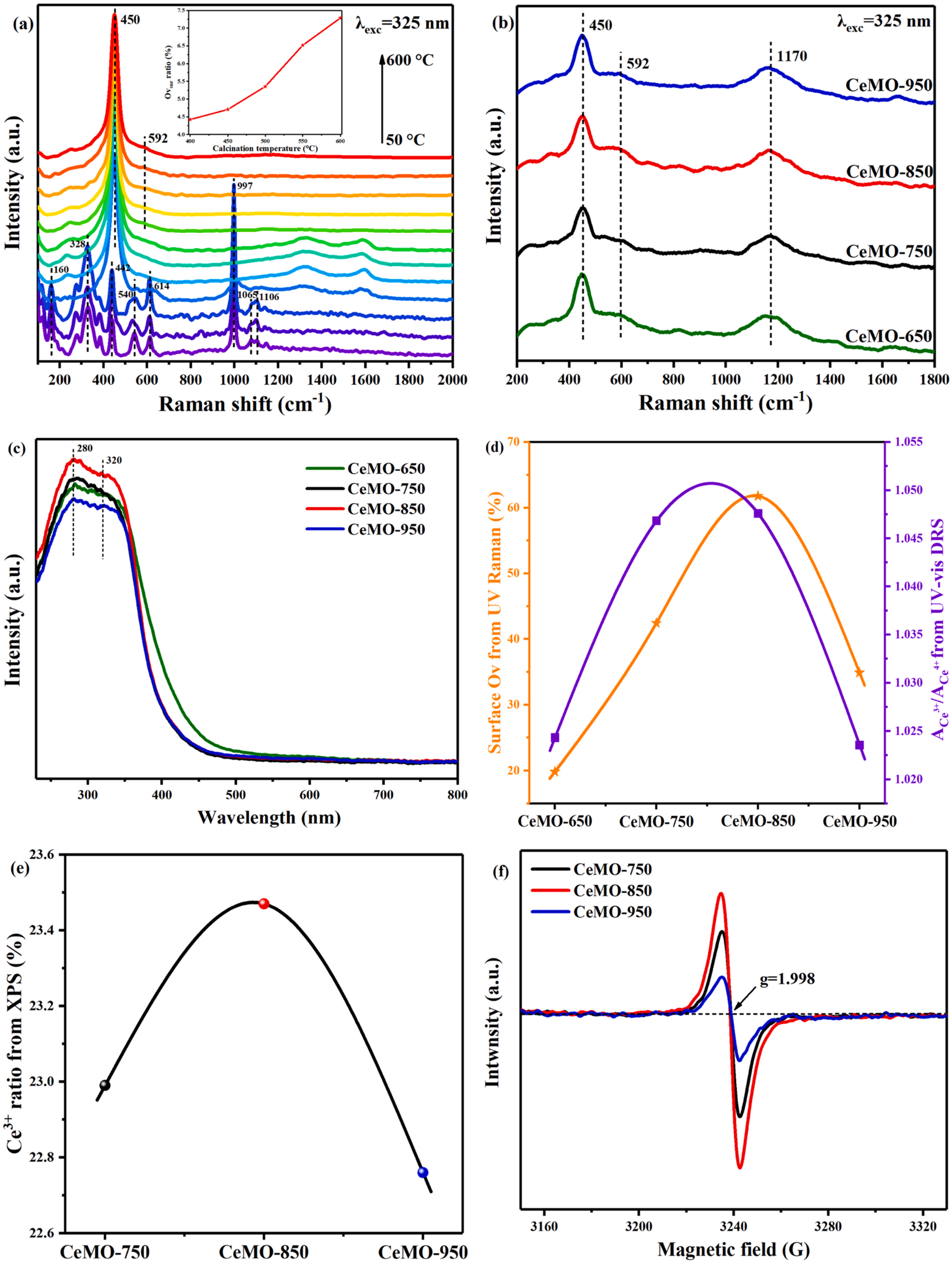

Fig. 5. (a) *In situ* UV Raman spectra of the Ce-LDH material during calcining from 50 °C to 600 °C under air (inset: surface Ov_{sur} ratio according to I_{592}/I_{450}). (b) UV Raman, (c) UV–vis DRS spectra, and (d) surface Ov and Ce^{3+} concentration plots of CeMO-650, CeMO-750, CeMO-850 and CeMO-950 samples. (e) Ce^{3+} ratio plots, and (f) ESR spectra of CeMO-750, CeMO-850 and CeMO-950 samples. (g) The proposed mechanism for the formation of oxygen vacancies during Ce-LDH pyrolysis.

zone sampling, to be a= 5.479 Å. We then use it to construct a $CeO_2(111)$ surface model with $p(3 \times 3)$ periodicity in the x and y directions and 3 stoichiometric layers in the z direction by vacuum depth of 15 Å in order to separate the surface slab from its periodic duplicates. This $CeO_2(111)$ surface model contains 27 Ce and 54 O atoms. In another model, one O atom on the outmost layer was removed in order to create an oxygen vacancy. During structural optimizations, the gamma point in the Brillouin zone was used for k-point sampling, and the bottom two stoichiometric layers were fixed while the top one was allowed to fully relax. The adsorption energy (Eads) of adsorbate A was

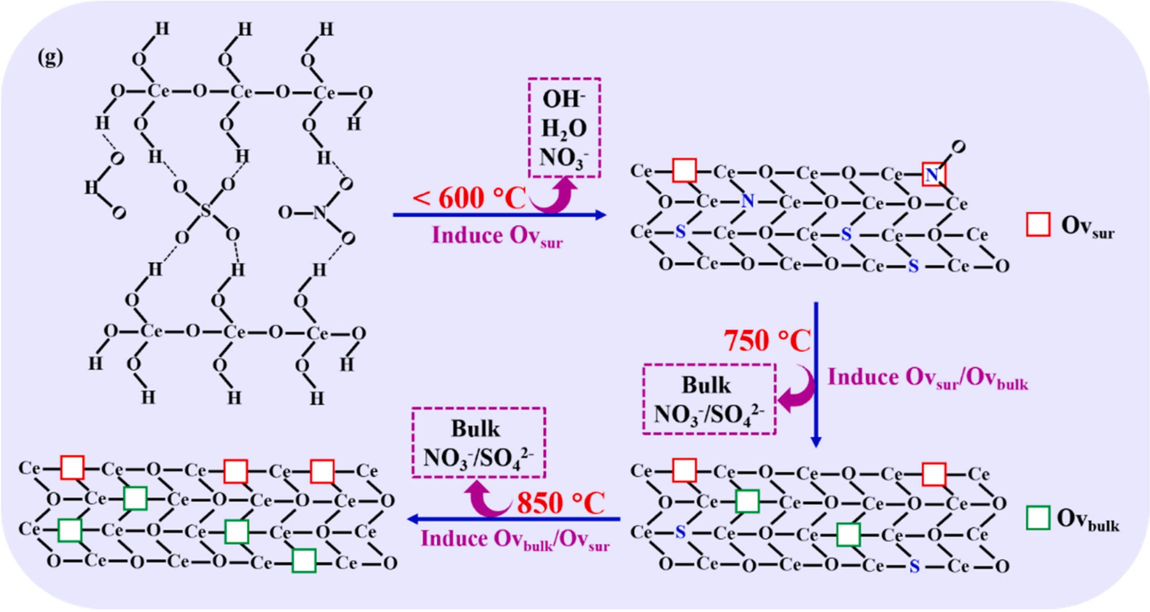

Fig. 5. (*continued*).

Table 2
The information of toluene desorption amount estimated by toluene-TPD.

Sample	Weak adsorption	Strong adsorption		A_{strong}/A_{weak}
	~200 °C	~250 °C	~300 °C	
CeMO-750	56.05%	31.06%	12.89%	0.78
CeMO-850	51.29%	34.58%	14.13%	0.95
CeMO-950	58.43%	30.34%	11.23%	0.71

defined as:

$E_{ads} = E_{A/polyimide} - E_{polyimide} - E_{A(g)}$where $E_{A/surf}$, E_{surf} and $E_{A(g)}$ are the energy of adsorbate A adsorbed on the polyimide, the energy of clean polyimide, and the energy of isolated A molecule in a cubic periodic box with a side length of 20 Å and a 1 × 1 × 1 Monkhorst-Pack k-point grid for Brillouin zone sampling, respectively.

2.4. *Evaluation of photocatalytic degradation toluene*

The photocatalytic oxidation of toluene test was carried out in a continuous flow stainless steel reactor equipped with a quartz opening window on the top under the 280 W Xe lamp irradiation. 50 mg of sample was evenly dispersed on a 400-mesh screen and placed in the reactor. A mixture of ~23 ppm toluene/air with a humidity of 20% RH was continuously introduced into the reactor. After dark treatment to reach the equilibrium state of toluene absorption and desorption, the photocatalytic reaction was done. The concentration of toluene and product CO_2 was monitored by gas chromatography (GC –7920). The formulas of toluene conversion rate and mineralization rate were given respectively by Eqs. (1) and (2):

$$Toluene\ conversion\left(\%\right) = \frac{[Toluene]_{in} - [Toluene]_{out}}{[Toluene]_{in}} \times 100\% \quad (1)$$

$$Toluene\ minerlization\left(\%\right) = \frac{[CO_2]_{out}}{7 \times [Toluene]_{in}} \times 100\% \quad (2)$$

where $[Toluene]_{in}$ and $[Toluene]_{out}$ are the inlet and outlet concentration (ppm) of toluene, respectively. $[CO_2]_{out}$ represent the outlet concentration (ppm) of product CO_2.

3. Results and discussion

3.1. *Morphological and structural properties*

The crystal structure and chemical composition of the as-prepared Ce-LDH were determined by XRD (Fig. S4a), FT-IR (Fig. S4b) and TG-MS (Fig. 1a). As shown in Fig. S4a, the sharp diffraction peaks observed in the low-angle region of Ce-LDH confirmed that it had a typical layered structure. Fig. S4b identified that the brucite-like layer -OH bonds as well as the interlayer water molecules, nitrate ion and sulfate ion existed in the Ce-LDH structure. The detailed description of FT-IR spectrum presented in the Supporting Information.

In order to obtain the calcining temperatures for Ce-LDH, the TG-MS curves of Ce-LDH were analyzed (Fig. 1a). The mass loss in the temperature range of 25–400 °C, 400–600 °C, 600–850 °C were attributed to the decomposition of interlayer water molecules/OH^-, nitrate ions, as well as interlayer sulfate ions, respectively, which matched well with the pattern of the LDH materials. According to the TG-MS curves of Ce-LDH, the calcining temperatures of 750, 850, 950 °C were chosen. Besides, the XRD results of CeMO-750, CeMO-850, and CeMO-950 suggested that the formation of CeO_2. In Fig. 1b, the characteristic peaks of the obtained CeMO samples could be perfectly indexed to cubic fluorite CeO_2, according to JCPDF No. 34-1002. Moreover, Ce and O elements were observed on all three CeMO catalysts surface (Fig. S5). Therefore, the CeO_2 (CeMO) photocatalysts via an anion-induced oxygen vacancy method were successfully synthesized.

The morphologies and microstructures of the CeMO products were systematically monitored by SEM, TEM, and AFM analysis. Obviously, the SEM images show that all CeMO materials display a platelet-like structure composed of uneven size (1–3 μm, 0.1–2 μm and 0.05–2 μm for CeMO-750, CeMO-850 and CeMO-950, respectively) and randomly stack nanosheets (Figs. 2a, S6). The TEM results (Figs. 2b, S7) suggested that the calcination temperature and the interlayer ions and OH^- removal led to some particles assembling CeO_2 nanosheets. Moreover, the AFM images clearly reflected that CeMO samples exhibited a stack of layers (Figs. 2c, S8), which agreed with the results of SEM. The thickness of CeMO-750, CeMO-850, and CeMO-950 are 5–35 nm, 10–60 nm, and 2–4 nm, respectively, which may be caused by the destruction of CeMO morphology, due to too high temperature. Combining the results of SEM, TEM, and AFM, it can be concluded that along with the increase in calcination temperature, CeMO nanosheets showed a reduced size and

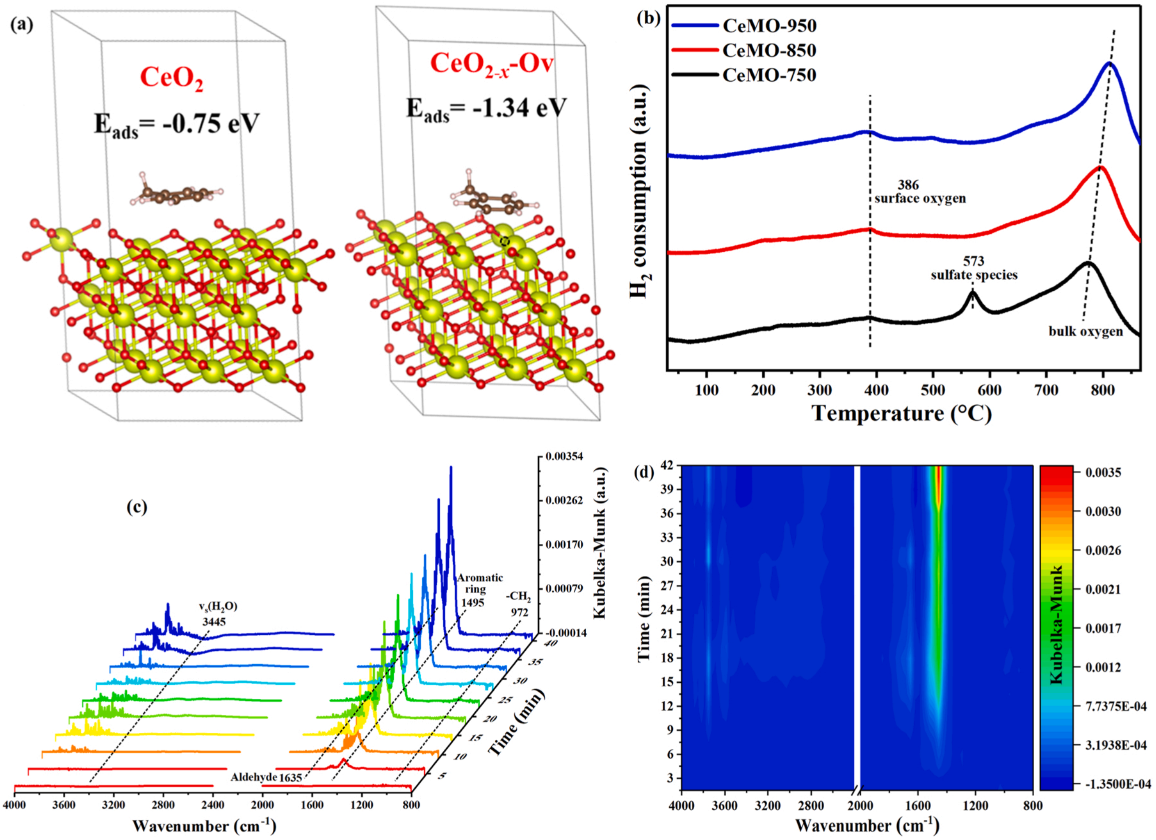

Fig. 6. (a) Calculated adsorption energy of toluene for CeO_2 (left) and CeO_{2-x} with Ov (right). (b) H_2-TPR profiles of CeMO-750, CeMO-850 and CeMO-950 samples. (c-d) *In situ* DRIFTS of toluene adsorption on CeMO-850 within 40 min at 30 °C in dark.

more irregular shape. Furthermore, the N_2 adsorption-desorption isotherms (Fig. S9a) of the CeMO samples show type IV with H1 hysteresis loop manifesting the presence of mesoporous structures, owing to the decomposition of interlayer anions during the calcination of Ce-LDH, which is consistent with the pore size distribution curves (Fig. S9b) [38]. As summarized in Table S1, all three CeMO samples possess similar specific surface area and pore size, which suggest that the difference in CeMO catalytic activity is not directly related to the specific area and pore size.

3.2. Photocatalytic performance for toluene degradation

Photocatalytic oxidation activity towards toluene under light irradiation as a function of time was evaluated and compared in Fig. 3 over the fabricated CeMO, CeO_2-H_2, P25, and common CeO_2 samples. Only 5% of toluene is oxidized after 3 h irradiation, so the self-photo decompose of toluene was negligible (Fig. 3a). As expected, the toluene conversion and mineralization results of the samples are in the same sequence as CeMO-850 > CeMO-750 > CeMO-950, and the performance of CeMO-850 is also better than that of the common CeO_2 (c-CeO_2) and even commercial P25. More importantly, the toluene mineralization rate of CeMO-850 is as high as 58%, while that of CeMO-750, CeMO-950, c-CeO_2, and commercial P25 are only 42%, 2%, 12%, 39%, respectively. In particular, compared with common method for producing oxygen vacancies by H_2 post-treatment (CeO_2-H_2), as-prepared CeO_2 nanosheets with rich oxygen vacancies through the anion-induced way showed outstanding photocatalytic performance for toluene oxidation. The photocatalytic performance of CeMO-850 is more excellent than that of other related photocatalysts in literature, summarizing in Table S2. Furthermore, the stabilities of CeMO catalysts were also determined in Fig. 3b-d. Surprisingly, the photocatalytic activities over CeMO-750 and CeMO-950 obviously decreased when reacting 9 h, while CeMO-850 was provided with the steady performance (Fig. 3b). Meanwhile, during the 12 h irradiation, CeMO-850 consistently maintained the highest toluene mineralization capacity (Fig. 3c). Besides, the conversion and mineralization rate towards toluene of CeMO-850 did not exhibit remarkable deterioration after three successive cycles of photocatalytic reaction (Fig. 3d). Therefore, the different activities and stabilities were revealed by the following characterizations.

3.3. The generation of reactive oxygen species (ROS)

In the process of efficient photocatalytic oxidation of toluene, the ability of photocatalysts to produce active oxygen radicals is the most decisive step. The generation ability of active oxygen radicals depends on the band structure of the semiconductor material, and the UV–vis DRS and valence band (VB) XPS were introduced to examine band gaps and VB position of CeMO samples (Fig. S10). According to the results in Fig. S10, we obtained the specific band structure of the CeMO materials and shown in Fig. 4a. The VB value of CeMO-850 (2.12 eV) is more positive than that of CeMO-750 (2.03 eV) and CeMO-850 (2.01 eV), while the CB value of CeMO-850 (−0.76 eV) is more negative than that of CeMO-750 (−0.69 eV) and CeMO-950 (−0.73 eV), suggesting that CeMO-850 possess a stronger ability to produce ROS. Additionally, the DMPO-ESR trapping technique was employed to directly identify the in-situ formed active oxygen radicals under light irradiation (Fig. 4b-c). Apparently, all three CeMO photocatalysts are able to generate ·OH and $\cdot O_2^-$ radicals, whereas the radicals signal intensities of CeMO-850 are much higher than those of CeMO-750 and CeMO-950. It visually suggested that CeMO-850 could produce more ROS participating in the photocatalytic oxidation process of toluene, thus exhibiting excellent toluene mineralization ability. Generally, the generation of ROS is closely related with surface oxygen species and photoelectric properties,

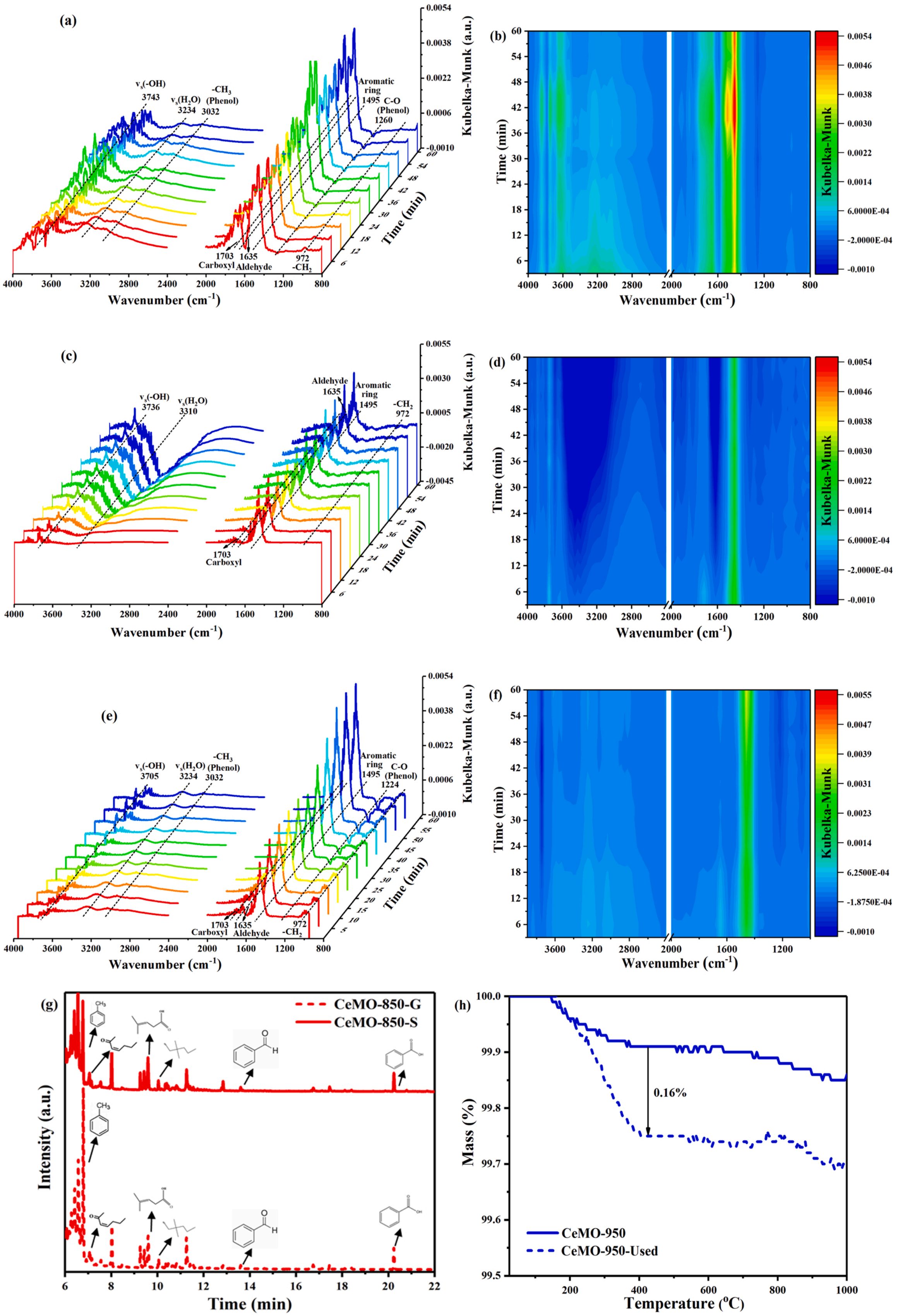

Fig. 7. *In situ* DRIFTS of toluene degradation on (a-b) CeMO-750, (c-d) CeMO-850, and (e-f) CeMO-950 within 60 min under Xe lamp irradiation. (g) The GC-MS spectra of photocatalyst surface (CeMO-850-S) and gas phase (CeMO-850-G) produced by CeMO-850 after photocatalytic oxidation of toluene for 3 h. (h) The TG profiles of CeMO-950 before and after the photo-oxidized toluene reaction.

Table 3
Intermediates identification of toluene photocatalytic oxidation by GC-MS.

Retention time (min)	*m/z*	Structural formula	Chemical name	Molecular formula
6.78	92	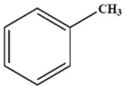	Toluene	C_7H_8
7.06	112	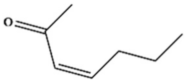	3-Hepten-2-one	$C_7H_{12}O$
9.59	114	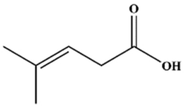	4-Methyl-3-pentenoic acid	$C_6H_{10}O_2$
10.04	116	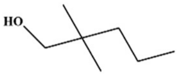	2, 2-Dimethyl-1-pentanol	$C_7H_{16}O$
13.61	106	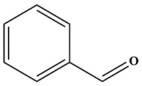	Benzaldehyde	C_7H_6O
20.24	122	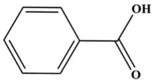	Benzoic acid	$C_7H_6O_2$

which were analyzed as followed.

The ·OH radicals are almost from the activation and oxidation of the surface adsorbed H_2O molecules and hydroxyls [39–41]. XPS spectra of O 1 s (Fig. 4d) were utilized to confirm more adsorbed oxygen species on CeMO-850 surface. For CeMO-850, the peaks at 532.3, 531.3 and 529.4 eV are indexed to adsorbed hydroxyl oxygen (O_H), chemisorbed oxygen species on the Ov (O_2^-, O_2^{2-}, or O^-) and lattices oxygen (O_L), respectively [26,29,42–44]. And the area ratios of O_H/O_{total} and O_v/O_{total} are ordered by CeMO-850 (26.90%, 39.76%) > CeMO-750 (22.79%, 33.73%) > CeMO-950 (19.47%, 30.97%). It was reasonably concluded that more adsorbed oxygen species on the CeMO-850 surface was oxidized by photogenerated carriers in favor of more ·OH and $\cdot O_2^-$ radicals formation, thus boosting the photocatalytic toluene mineralization. Interestingly, we found that the peak related to chemisorbed oxygen species on the Ov (O_2^-, O_2^{2-}, or O^-) of CeMO-850 shifted toward the higher binding energy compared with CeMO-750 and CeMO-950, indicating of chemisorbed oxygen species with less electrons on CeMO-850, i.e., O_2^-. According to literatures [45,46], O_2^- species can promote toluene deep oxidation. Therefore, CeMO-850 was provided with better activity of toluene oxidation. Moreover, the oxygen species of as-prepared samples were further evaluated by O_2-TPD (Fig. 4e). Three oxygen desorption regions (< 300 °C, 300–600 °C, > 600 °C) were discovered for the CeMO photocatalysts, which were related to the desorption of surface adsorbed oxygen, surface lattice oxygen, and bulk lattice oxygen, respectively [47]. Interestingly, it could be clearly seen that CeMO-850 had more chemical adsorbed oxygen (200–300 °C) leading to stronger oxygen utilization ability, which was conducive to the generation of ·OH. In addition, CeMO-850 exhibited a lower desorption temperature in the mid-temperature region, indicating that its active oxygen mobility was higher, which was beneficial to the replenishment of reactive oxygen species during the photooxidation of toluene. Importantly, the acid sites are also regarded as the active sites for generating ROS on the surface of catalyst. Herein, Py-IR adsorption spectra were determined to distinguish the Lewis (L) acid sites and Brønsted (B) acid sites of the CeMO samples (Fig. 4f). The bands emerged at 1540 and 1637 cm^{-1} were attributed to pyridine adsorbed on B acid sites, the peaks at 1445, 1575, and 1607 cm^{-1} were related to pyridine adsorbed on L acid sites [48,49]. And the peak located at 1490 cm^{-1} was corresponded with sum of B and L acid sites [49]. The quantitative results of Py-IR listed in Table 1 and showed that CeMO-850 possessed more B acid sites on Ce^{3+} sites donating protons compared with CeMO-750 and CeMO-950, which was favorable for the formation of ·OH and provided higher photocatalytic oxidation efficiency of toluene [50].

In addition, the $\cdot O_2^-$ radicals are closely related to oxygen vacancies (Ov) and oxygen mobility, and *in situ* UV Raman, the XPS spectra of Ce 3d, UV Raman, UV–vis DRS and ESR spectra were used to study the formation mechanism of Ov. The in-situ UV Raman (Fig. 5a) showed the change of surface species and the surface Ov formation in the pyrolysis process of Ce-LDH. As shown in Fig. 5a, when the calcination temperature was lower than 200 °C, Ce-LDH remained the structure of hydrotalcite with the peaks around at 160, 328, 442, 540, 614, 997, 1065, and 1106 cm^{-1} corresponding to H_2O/OH^-, hydrogen-bond, Ce^{4+}-O, Ce^{3+}-O, SO_4^{2-}, and NO_3^-, respectively [51–54]. The main peak located at 450 cm^{-1} was characteristic of F_{2g} band. Specially, the band at 592 cm^{-1} was related to the vibration of oxygen vacancy [53]. With the

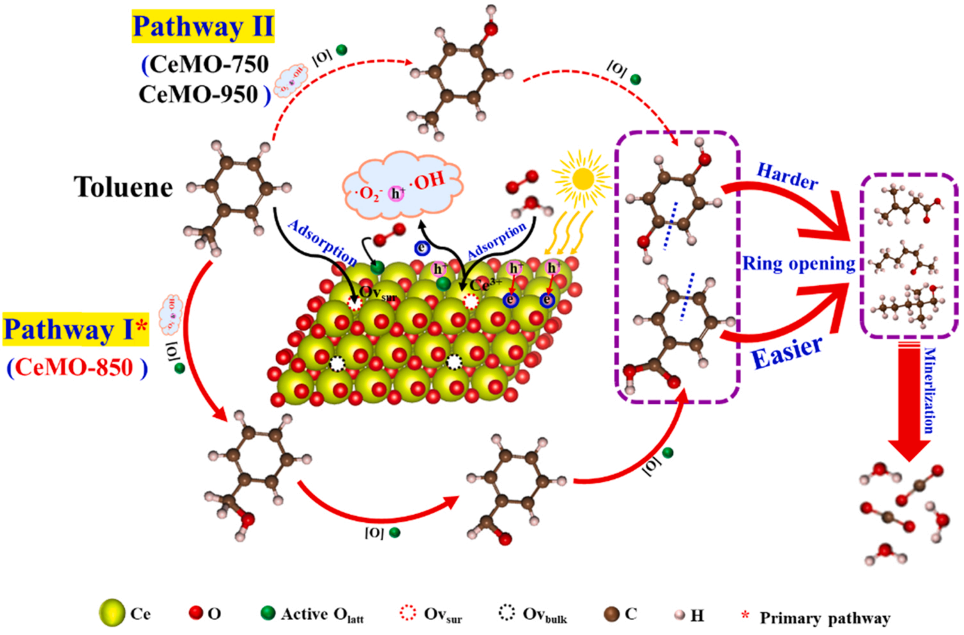

Fig. 8. The proposed mechanism for photocatalytic oxidation of toluene on CeMO.

increase of the Ce-LDH pyrolysis temperature ($< 600\ ^{\circ}C$), the removal of OH^{-}/H_2O and a handful of NO_3^{-} induced the continuous increase of surface Ov (I_{592}/I_{450}). Therefore, the removal of OH^{-}/H_2O and nitrate would take away the attached oxygen atom of CeO_2, leading to the generation of Ov. Due to the limitation of the heating conditions of the *in-situ* Raman reaction cell, the highest temperature can only be measured at 600 °C. The effects of sulfate and nitrate ions removal on Ov were investigated as followed. The Ov of CeMO-650, CeMO-750, CeMO-850, and CeMO-950 were determined in Fig. 5b-f. The UV Raman and XPS spectra were employed to investigate the surface oxygen vacancy (Ov_{sur}). The detailed UV Raman (Fig. 5b) and Ce 3d XPS spectra (Fig. S11) was analyzed, and the corresponding concentration of Ov_{sur} and content of Ce^{3+} (Ce^{3+} / (Ce^{3+} + Ce^{4+})) were calculated in Fig. 5d and Fig. 5e. It showed that the largest concentration of Ov_{sur} was CeMO-850. Combined the result of TG-MS, it was proposed that when the pyrolysis temperature was lower than 600 °C, the removal of OH^{-}/H_2O and nitrate ions induced the continuous increase of Ov_{sur}. Besides, the high temperature would make the bulk active oxygen atom migrate to the surface, and thus Ov_{sur} were more on CeMO-850 than CeMO-750, agreement with the results of XPS (Fig. 5e). In addition, the UV–vis DRS (Fig. 5c-d) and ESR (Fig. 5f) results showed the total concentration, including of surface and bulk [29,55]. In UV–vis DRS spectra (Fig. 5c), two absorption band at 280 and 320 nm are related to the absorptions of Ce^{3+} and Ce^{4+}, respectively [29]. The corresponding ratios of Ce^{3+} to Ce^{4+} were calculated in the Fig. 5d. The UV–vis DRS (Ce^{3+} ratio) and ESR ($g = 1.998$) results suggested that the total concentration of Ov was ordered by CeMO-850 > CeMO-750 > CeMO-950. Combined the TG-MS results, it was showed that the nitrate and sulfate ions in bulk decomposed between 700 and 850 °C, leading to the formation of bulk oxygen vacancy (Ov_{bulk}). The signal of bulk sulfate ions in the H_2-TPR results further confirmed that few bulk sulfate ions in CeMO-750, leading to fewer Ov_{bulk}. Therefore, the process and mechanism on the generation of oxygen vacancies on CeO_2 nanosheets via the anion-induced Ce-LDH pyrolysis method were proposed in Fig. 5g to explain the richer oxygen vacancies on CeMO-850. The higher concentration of Ov and Ce^{3+} in CeMO-850 sample could effectively capture toluene and gaseous oxygen, respectively, which facilitated the activation of O_2 molecules, and constructed more $\cdot O_2^{-}$ radicals. Therefore, CeMO-850 with more Ov had richer ·OH and $\cdot O_2^{-}$, which were recognized as important ROS for ring opening in the photooxidation process of toluene, and became one of the reasons for the best photocatalytic performance.

Furthermore, the formation of ROS also depends on the available photo-generated charges. Therefore, the photoelectric properties of the photocatalyst were determined. Fig. 5c revealed that CeMO-850 with abundant Ov had stronger light response capacity, and thus promoted the generation of more photogenerated charges [9]. The photoexcited carries transfer and separation efficiency were detected by EIS (Fig. S12a), PL (Fig. S12b), and transient photocurrent response (Fig. S12c), and ranked by CeMO-850 > CeMO-750 > CeMO-950. On the basis of that, more photogenerated electron-hole pairs were on CeMO-850 to effectively participate in the generation of ROS, thereby achieving excellent photocatalytic performance.

3.4. Toluene adsorption and activation capacity

As we all know, the adsorption of reactant molecules on the catalyst surface is the prerequisite in heterogeneous catalytic reactions. The toluene adsorption kinetic and desorption process were determined by the TGA experiment (Fig. S13). It can be observed that CeMO-850 has higher adsorption and lower desorption capacity for toluene with respect to CeMO-750 and CeMO-950, hinting that toluene can be efficiently adsorbed and activated on the surface of CeMO-850, which might be resulted from its higher Ov concentration. An insight into toluene adsorption properties was further measured by toluene-TPD. As depicted in Fig. S14, the toluene-TPD spectra of CeMO samples were fitted and attributed to weak ($< 200\ ^{\circ}C$) and strong adsorption (200–400 °C), respectively. It was reported that when the photocatalyst was exposed to toluene atmosphere, toluene will preferentially bond on the strong adsorption sites, and then adsorb on the weak adsorption sites [56]. The π bond of toluene as electron donor tend to combine with electron-deficient Ov or OH groups to form strong Ov-π/OH-π bonds, so that this kind of toluene species is strongly adsorbed on the catalyst surface to further activated and mineralized efficiently, which is widely recognized as an effective adsorption way [57–59]. Besides, the weak adsorption was considered as ortho-, meta-, and para-H atoms of toluene interacting with the OH groups on catalysts, forming weak HO…H bonds [58,60]. However, the weakly adsorbed toluene is easily desorbed before it can be activated or even converted, and the photooxidation process of toluene is terminated. Based on the peaks area ratios of A_{strong}/A_{total} (Table 2), i.e., CeMO-850 (48.71%) > CeMO-750 (43.95%) > CeMO-950 (41.57%), it is reasonable to conclude that larger amount of strongly adsorbed toluene on the CeMO-850 is conducive to outstanding photocatalytic activity of toluene. For the purpose of certifying this hypothesis, the toluene adsorption energy (E_{ads}) on the surface of CeO_2 and $CeO_{2\text{-}x}$ with Ov ($CeO_{2\text{-}x}$-Ov) were calculated by DFT method (Fig. 6a). The E_{ads} value of $CeO_{2\text{-}x}$-Ov (−1.34 eV) is relatively lower than that of CeO_2 (−0.75 eV), revealing the existence of Ov is more conducive to the adsorption and activation of toluene, which might result from the Ov acting as sites to adsorb toluene via π electrons (benzene rings) to Ov. Therefore, CeMO-850 with more Ov had the best ability to adsorption and activation for toluene.

In addition, XRF and H_2-TPR profiles explained the poorer performance of CeMO-750. The results of XRF (Table S3) show that 0.1% sulfur (S) are present in CeMO-750, while absent in the CeMO-850 and CeMO-950. In H_2-TPR, apart from the reduction of surface oxygen (~ 386 °C) and bulk oxygen (> 750 °C) species, CeMO-750 also shows obvious reduction of sulfate species (~ 573 °C) in Fig. 6b, which is consistent with the result of XRF [61]. These sulfate species from incomplete decomposition of Ce-LDH could occupy the adsorption and reaction sites, and thereby significantly reduced the catalytic activity of CeMO-750.

Furthermore, in situ DRIFTS experiments of toluene adsorption on CeMO were further used to investigate the dynamic evolution process of toluene adsorption and activation. The in situ DRIFTS results were all uniformly normalized. After injecting 20 ppm toluene/air to reaction cell, the intensity of the typical toluene absorption peak (1495 cm^{-1}) on CeMO-850 (Fig. 6c-d) gradually increases and stabilizes within 30 min [2], which is higher than that of CeMO-750 (Fig. S15a-b) and CeMO-950 (Fig. S15c-d), because of richer O_{Vsur} on CeMO-850. For CeMO-850, the two weak bands assigned to benzoic acid are observed at 1635 and 972 cm^{-1}, and the negative band related to isolated $\nu_s(H_2O)$ at 3445 cm^{-1}, indicating that a small amount of adsorbed toluene are oxidized [62–64]. While, on CeMO-750 and CeMO-950, a new peak assigned to benzaldehyde (1703 and 972 cm^{-1}) emerges at 1703 cm^{-1} [65]. The different peak and the intensity evidently showed that CeMO-850 with more Ov_{sur} had stronger toluene adsorption and activation ability at room temperature in dark, leading to further opening rings of toluene under light irradiation.

3.5. Photocatalytic reaction mechanism

To elucidate the reaction pathways and the intermediates accumulated on the as-prepared CeMO sample, *in situ* DRIFTS of toluene oxidation under Xe lamp irradiation and GC-MS were carried out and presented in Fig. 7a-g. With the increase of irradiation time, some new species including polymerized or isolated -OH groups (3743, 3736 and 3705 cm^{-1}) and cresol (3032, 1260 and 1224 cm^{-1}) appear and keep accumulating on CeMO-750 (Fig. 7a-b) and CeMO-950 (Fig. 7e-f) [66–69], not on CeMO-850. Notably, only the small number of intermediates (benzaldehyde and benzoic acid) and a relatively broad peak of water desorption are discovered over CeMO-850 (Fig. 7c-d), revealing its high-efficiency toluene mineralization ability owing to abundant Ov$_{bulk}$. However, a large number of accumulated intermediates (cresol, benzaldehyde and benzoic acid) are detected on CeMO-750, and more adsorbed -OH not activated into ·OH on CeMO-750, showing their declined activity and inactivation. In addition, although the toluene conversion of CeMO-950 is extremely low, there are still various intermediate products, which speculate that lots of coke deposit on the CeMO-950 photocatalyst surface, leading to its poor stability.

Moreover, GC-MS test was designed to identify the by-products accumulated on the used photocatalyst surface (marked as CeMO-S) and gas phase (marked as CeMO-G) in Figs. 7g, S16 and Table 3. It can be clearly seen that the by-products are detected in the exhaust gas and on the surface of CeMO-750 and CeMO-850 after 3 h of photocatalytic reaction, which attribute to its high toluene conversion ability. On the contrary, extremely few ring-opening intermediates are observed in the gas phase, while various by-products are deposited on the surface of CeMO-950, showing that the fairly poor toluene photodegradation performance and severe carbon species accumulation, confirmed by the TG results. In Fig. 7h, the weight loss of 0.16% stemmed from by-products deposition is observed in the used CeMO-950, which is good agreement with the results of *in situ* DRIFTS of toluene oxidation. Therefore, CeMO-950 had poor stability, due to by-products deposition poisoning the catalyst.

According to the results of in situ DRIFTS and GC-MS, the possible mechanisms of photocatalytic toluene oxidation over CeMO were proposed, compared, and depicted in Fig. 8.

Firstly, under the light irradiation, the oxygen-containing species captured easily by Ce^{3+} sites were reduced to produce $\cdot O_2^-$ radicals by photogenerated electrons (e^-) and oxidized into ·OH radicals by the holes (h^+) [70]. Secondly, the toluene adsorbed on the oxygen vacancies could be attacked fast by active species ($\cdot O_2$, ·OH and h^+), and the subsequent toluene oxidation process could be as follow: (I) the methyl dehydrogenation pathway: toluene was gradually oxidized to benzyl alcohol, benzaldehyde and benzoic acid; and (II) aromatic ring dehydrogenation reaction pathway: the hydrogen atoms on the aromatic ring of toluene were extracted to form into cresol and then into hydroquinone. Generally, mineralization of benzoic acid (pathway I) is much easier than that of hydroquinone (pathway II) [71]. Based on photocatalytic toluene on CeMO-850 mainly following pathway I, while pathway I and II observed on CeMO-750 and CeMO-950, owing to the existence of few sulfate ions and coke species, therefore, CeMO-850 was provided with the best photocatalytic performance of toluene oxidation, and its reaction mechanism was that aromatic compounds were transferred into the ring-opening intermediates (i.e., 3-hepten-2-one, 4-methyl-3-pentenoic acid, 2, 2-dimethyl-1-pentanol, etc.), and finally were mineralized into CO_2 and H_2O in Fig. 8. Interestingly, the different reaction routes of photocatalytic toluene oxidation were related on the Ov, i.e., Ov$_{sur}$ with Ce^{3+} species were beneficial for toluene adsorption, B acid sites and ·OH radical generation, respectively, and Ov$_{bulk}$ was helpful for oxygen mobility and deep mineralization. In comparison with published studies supplied in Table S4, we identified some ring-opening intermediates as well as revealed oxygen vacancies playing an important role in photocatalytic toluene oxidation.

4. Conclusions

Overall, the CeMO samples with different concentration of oxygen vacancies were successfully obtained via an anion-induced method. Compared with CeMO-750 and CeMO-950, the as-synthesized CeMO-850 with more Ov$_{sur}$ and Ov$_{bulk}$ possesses the best activity, due to advantageous B acid sites, active oxygen species, toluene adsorption, and photo-generated charges, and thus plentiful ROS ($\cdot O_2^-$ and ·OH) promote open rings of aromatic intermediates and increase toluene mineralization. While CeMO-750 with fewer sulfate ions is bad for toluene adsorption and activation, and CeMO-950 with less Ov is easier to be poisoned. Furthermore, the different reaction pathways showed the various toluene mineralization ability. The anion-induced oxygen vacancy strategy provides a new perspective for introducing uniform oxygen vacancy defects in photocatalysts.

CRediT authorship contribution statement

Weixin Zou, Bin Gao and Lin Dong proposed the research and supervised the project. Xiaoqian Wei designed and conducted the experiments and analyzed the experimental results as well as wrote the manuscript. Ke Li, Jiawei Ji and Yandi Cai synthesized the target CeO_2 nanosheets photocatalysts with various oxygen vacancies. Xueyang Zhang, Yandi Cai and Jiawei Ji performed the physicochemical and photochemical characterization of as-synthesized materials. Qing Tong organized data, including research literature and drawing. All authors discussed the results and commented on the manuscript.

Declaration of Competing Interest

The authors declare that they have no known competing financial interests or personal relationships that could have appeared to influence the work reported in this paper.

Data Availability

Data will be made available on request.

Acknowledgments

W.Z., L.D. and Q.T. would like to acknowledge the support of Fundamental Research Funds for the Central Universities (21114380163) and the National Natural Science Foundation of China (21972062, 22106067).

Appendix A. Supplementary material

Supplementary data associated with this article can be found in the online version at doi:10.1016/j.apcatb.2022.121694.

References

[1] C. Lai, Z. Wang, L. Qin, Y. Fu, B. Li, M. Zhang, S. Liu, L. Li, H. Yi, X. Liu, X. Zhou, N. An, Z. An, X. Shi, C. Feng, Metal-organic frameworks as burgeoning materials for the capture and sensing of indoor VOCs and radon gases, Coord. Chem. Rev. 427 (2021) 213565–213580, https://doi.org/10.1016/j.ccr.2020.213565.

[2] J. Liu, P. Wang, W. Qu, H. Li, L. Shi, D. Zhang, Nanodiamond-decorated ZnO catalysts with enhanced photocorrosion-resistance for photocatalytic degradation of gaseous toluene, Appl. Catal. B Environ. 257 (2019) 117880–117888, https://doi.org/10.1016/j.apcatb.2019.117880.

[3] X. Zhang, X. Miao, W. Xiang, J. Zhang, C. Cao, H. Wang, X. Hu, B. Gao, Ball milling biochar with ammonia hydroxide or hydrogen peroxide enhances its adsorption of phenyl volatile organic compounds (VOCs), J. Hazard. Mater. 403 (2021) 123540–123549, https://doi.org/10.1016/j.jhazmat.2020.123540.

[4] J. Kong, G. Li, M. Wen, J. Chen, H. Liu, T. An, The synergic degradation mechanism and photothermocatalytic mineralization of typical VOCs over PtCu/CeO_2 ordered porous catalysts under simulated solar irradiation, J. Catal. 370 (2019) 88–96, https://doi.org/10.1016/j.jcat.2018.12.003.

[5] L. Chen, W. Cui, J. Li, H. Wang, Xa Dong, P. Chen, Y. Zhou, F. Dong, The high selectivity for benzoic acid formation on $Ca_2Sb_2O_7$ enables efficient and stable toluene mineralization, Appl. Catal. B Environ. 271 (2020) 118948–118957, https://doi.org/10.1016/j.apcatb.2020.118948.

[6] S. Zhou, Y. Wang, K. Zhou, D. Ba, Y. Ao, P. Wang, In-situ construction of Z-scheme g-C_3N_4/WO_3 composite with enhanced visible-light responsive performance for nitenpyram degradation, Chin. Chem. Lett. 32 (2021) 2179–2182, https://doi.org/10.1016/j.cclet.2020.12.002.

[7] Y. Huang, Y. Yu, Y. Yu, B. Zhang, Oxygen vacancy engineering in photocatalysis, Sol. RRL 4 (2020) 2000037–2000050, https://doi.org/10.1002/solr.202000037.

[8] K. Zhu, F. Shi, X. Zhu, W. Yang, The roles of oxygen vacancies in electrocatalytic oxygen evolution reaction, Nano Energy 73 (2020) 104761–104778, https://doi.org/10.1016/j.nanoen.2020.104761.

[9] Y. Sun, H. Wang, Q. Xing, W. Cui, J. Li, S. Wu, L. Sun, The pivotal effects of oxygen vacancy on Bi_2MoO_6: Promoted visible light photocatalytic activity and reaction

mechanism, Chin. J. Catal. 40 (2019) 647–655, https://doi.org/10.1016/S1872-2067(19)63277-8.

[10] S. Gong, F. Rao, W. Zhang, Q. Hassan, Z. Liu, J. Gao, J. Lu, M. Hojamberdiev, G. Zhu, Au nanoparticles loaded on hollow BiOCl microstructures boosting CO_2 photoreduction, Chin. Chem. Lett. (2021), https://doi.org/10.1016/j.cclet.2021.12.039.

[11] W. Zou, B. Deng, X. Hu, Y. Zhou, Y. Pu, S. Yu, K. Ma, J. Sun, H. Wan, L. Dong, Crystal-plane-dependent metal oxide-support interaction in CeO_2/g-C_3N_4 for photocatalytic hydrogen evolution, Appl. Catal. B Environ. 238 (2018) 111–118, https://doi.org/10.1016/j.apcatb.2018.07.022.

[12] B. Lei, W. Cui, J. Sheng, H. Wang, P. Chen, J. Li, Y. Sun, F. Dong, Synergistic effects of crystal structure and oxygen vacancy on Bi_2O_3 polymorphs: intermediates activation, photocatalytic reaction efficiency, and conversion pathway, Sci. Bull. 65 (2020) 467–476, https://doi.org/10.1016/j.scib.2020.01.007.

[13] H. Li, Y. Gao, D. Gao, Y. Wang, Effect of oxide defect on photocatalytic properties of $MSnO_3$ (M = Ca, Sr, and Ba) photocatalysts, Appl. Catal. B Environ. 243 (2019) 428–437, https://doi.org/10.1016/j.apcatb.2018.10.076.

[14] Y. Li, W. Zhang, J. Niu, Y. Chen, Mechanism of photogenerated reactive oxygen species and correlation with the antibacterial properties of engineered metal-oxide nanoparticles, ACS Nano 6 (2012) 5164–5173, https://doi.org/10.1021/nn300934k.

[15] M. Shen, T. Ding, S.T. Hartman, F. Wang, C. Krucylak, Z. Wang, C. Tan, B. Yin, R. Mishra, M.D. Lew, B. Sadtler, Nanoscale colocalization of fluorogenic probes reveals the role of oxygen vacancies in the photocatalytic activity of tungsten oxide nanowires, ACS Catal. 10 (2020) 2088–2099, https://doi.org/10.1021/acscatal.9b04481.

[16] M. Li, P. Wang, Z. Ji, Z. Zhou, Y. Xia, Y. Li, S. Zhan, Efficient photocatalytic oxygen activation by oxygen-vacancy-rich CeO_2-based heterojunctions: synergistic effect of photoexcited electrons transfer and oxygen chemisorption, Appl. Catal. B Environ. 289 (2021) 120020–120030, https://doi.org/10.1016/j.apcatb.2021.120020.

[17] X. Chen, S. Zhan, D. Chen, C. He, S. Tian, Y. Xiong, Grey Fe-$CeO_{2-\sigma}$ for boosting photocatalytic ozonation of refractory pollutants: roles of surface and bulk oxygen vacancies, Appl. Catal. B Environ. 286 (2021) 119928–119941, https://doi.org/10.1016/j.apcatb.2021.119928.

[18] W. Zou, Y. Shao, Y. Pu, Y. Luo, J. Sun, K. Ma, C. Tang, F. Gao, L. Dong, Enhanced visible light photocatalytic hydrogen evolution via cubic CeO_2 hybridized g-C_3N_4 composite, Appl. Catal. B Environ. 218 (2017) 51–59, https://doi.org/10.1016/j.apcatb.2017.03.085.

[19] D. Wang, F. Yin, B. Cheng, Y. Xia, J. Yu, W. Ho, Enhanced photocatalytic activity and mechanism of CeO_2 hollow spheres for tetracycline degradation, Rare Met. 40 (2021) 2369–2380, https://doi.org/10.1007/s12598-021-01731-2.

[20] M. Noor, M.A. Al Mamun, A.K.M. Atique Ullah, A. Matsuda, G. Kawamura, M. A. Hakim, M.F. Islam, M.A. Matin, Physics of $Ce^{3+}\leftrightarrow Ce^{4+}$ electronic transition in phytosynthesized CeO_2/$CePO_4$ nanocomposites and its antibacterial activities, J. Phys. Chem. Solids 148 (2021) 109751–109760, https://doi.org/10.1016/j.jpcs.2020.109751.

[21] M. Wu, Y. Zhang, W. Szeto, W. Pan, H. Huang, D. Leung, Vacuum ultraviolet (VUV)-based photocatalytic oxidation for toluene degradation over pure CeO_2, Chem. Eng. Sci. 200 (2019) 203–213, https://doi.org/10.1016/j.ces.2019.01.056.

[22] Y. Zhang, Z. Li, L. Zhang, L. Pan, X. Zhang, L. Wang, A. Fazal e, J. Zou, Role of oxygen vacancies in photocatalytic water oxidation on ceria oxide: experiment and DFT studies, Appl. Catal. B Environ. 224 (2018) 101–108, https://doi.org/10.1016/j.apcatb.2017.10.049.

[23] J. Kong, Z. Xiang, G. Li, T. An, Introduce oxygen vacancies into CeO_2 catalyst for enhanced coke resistance during photothermocatalytic oxidation of typical VOCs, Appl. Catal. B Environ. 269 (2020) 118755–118763, https://doi.org/10.1016/j.apcatb.2020.118755.

[24] H. Yu, J. Li, Y. Zhang, S. Yang, K. Han, F. Dong, T. Ma, H. Huang, Three-in-one oxygen vacancies: whole visible-spectrum absorption, efficient charge separation, and surface site activation for robust CO_2 photoreduction, Angew. Chem. Int. Ed. Engl. 58 (2019) 3880–3884, https://doi.org/10.1002/anie.201813967.

[25] J. Xu, M. Li, L. Yang, J. Qiu, Q. Chen, X. Zhang, Y. Feng, J. Yao, Synergy of Ni dopant and oxygen vacancies in ZnO for efficient photocatalytic depolymerization of sodium lignosulfonate, Chem. Eng. J. 394 (2020) 125050–125059, https://doi.org/10.1016/j.cej.2020.125050.

[26] H. Xu, C. Shan, X. Wu, M. Sun, B. Huang, Y. Tang, C. Yan, Fabrication of layered double hydroxide microcapsules mediated by cerium doping in metal–organic frameworks for boosting water splitting, Energy Environ. Sci. 13 (2020) 2949–2956, https://doi.org/10.1039/D0EE02113J.

[27] M. Anjum, J. Zhao, V. Asl, M. Malik, G. Yasin, W. Khan, Green corrosion inhibitors intercalated Mg:Al layered double hydroxide coatings to protect Mg alloy, Rare Met. 40 (2021) 2254–2265, https://doi.org/10.1007/s12598-020-01538-7.

[28] Z. Huang, P. Wu, B. Gong, Y. Fang, N. Zhu, Fabrication and photocatalytic properties of a visible-light responsive nanohybrid based on self-assembly of carboxyl graphene and ZnAl layered double hydroxides, J. Mater. Chem. A 2 (2014) 5534–5540, https://doi.org/10.1039/C3TA15350A.

[29] T. Ye, W. Huang, L. Zeng, M. Li, J. Shi, CeO_{2-x} platelet from monometallic cerium layered double hydroxides and its photocatalytic reduction of CO_2, Appl. Catal. B Environ. 210 (2017) 141–148, https://doi.org/10.1016/j.apcatb.2017.03.051.

[30] C. Chen, H. Zeng, M. Yi, G. Xiao, S. Xu, S. Shen, B. Feng, In-situ growth of Ag_3PO_4 on calcined Zn-Al layered double hydroxides for enhanced photocatalytic degradation of tetracycline under simulated solar light irradiation and toxicity assessment, Appl. Catal. B Environ. 252 (2019) 47–54, https://doi.org/10.1016/j.apcatb.2019.03.083.

[31] G. Kresse, J. Furthmuller, Efficiency of ab-initio total energy calculations for metals and semiconductors using a plane-wave basis set, Comput. Mater. Sci. 6 (1996) 15–50, https://doi.org/10.1016/0927-0256(96)00008-0.

[32] G. Kresse, J. Furthmuller, Efficient iterative schemes for ab initio total-energy calculations using a plane-wave basis set, Phys. Rev. B 54 (1996) 11169–11186, https://doi.org/10.1103/PhysRevB.54.11169.

[33] J. Perdew, K. Burke, M. Ernzerhof, Generalized gradient approximation made simple, Phys. Rev. Lett. 77 (1996) 3865–3868, https://doi.org/10.1103/PhysRevLett.77.3865.

[34] G. Kresse, D. Joubert, From ultrasoft pseudopotentials to the projector augmented-wave method, Phys. Rev. B 59 (1999) 1758–1775, https://doi.org/10.1103/PhysRevB.59.1758.

[35] P. Blöchl, Projector augmented-wave method, Phys. Rev. B Condens. Matter 50 (1994) 17953–17979, https://doi.org/10.1103/PhysRevB.50.17953.

[36] S. Dudarev, G. Botton, S. Savrasov, C. Humphreys, A. Sutton, Electron-energy-loss spectra and the structural stability of nickel oxide: an LSDA1U study, Phys. Rev. B 57 (1998) 1505–1509, https://doi.org/10.1103/PhysRevB.57.1505.

[37] S. Grimme, J. Antony, S. Ehrlich, H. Krieg, A consistent and accurate ab initio parametrization of density functional dispersion correction (DFT-D) for the 94 elements H-Pu, J. Chem. Phys. 132 (2010) 154104–154122, https://doi.org/10.1063/1.3382344.

[38] C. Silva, Y. Bouizi, V. Forneś, H. García, Layered double hydroxides as highly efficient photocatalysts for visible light oxygen generation from water, J. Am. Chem. Soc. 131 (2009) 13833–13839, https://doi.org/10.1021/ja905467v.

[39] X. Dong, Z. Cui, Y. Sun, F. Dong, Humidity-independent photocatalytic toluene mineralization benefits from the utilization of edge hydroxyls in layered double hydroxides (LDHs): a combined operando and theoretical investigation, ACS Catal. 11 (2021) 8132–8139, https://doi.org/10.1021/acscatal.1c01599.

[40] X. Wei, X. Wang, Y. Pu, A. Liu, C. Chen, W. Zou, Y. Zheng, J. Huang, Y. Zhang, Y. Yang, M. Naushad, B. Gao, L. Dong, Facile ball-milling synthesis of CeO_2/g-C_3N_4 Z-scheme heterojunction for synergistic adsorption and photodegradation of methylene blue: characteristics, kinetics, models, and mechanisms, Chem. Eng. J. 420 (2021) 127719–127728, https://doi.org/10.1016/j.cej.2020.127719.

[41] G. He, J. Ma, B. Chu, R. Hu, H. Li, M. Gao, Y. Liu, Y. Wang, Q. Ma, P. Xie, G. Zhang, X. Zeng, J. Francisco, H. He, Generation and release of OH radicals from the reaction of H_2O with O_2 over soot, Angew. Chem. Int. Ed. (2022), e202201638, https://doi.org/10.1002/anie.202201638.

[42] W. Tan, A. Liu, S. Xie, Y. Yan, T.E. Shaw, Y. Pu, K. Guo, L. Li, S. Yu, F. Gao, F. Liu, L. Dong, Ce-Si mixed oxide: a high sulfur resistant catalyst in the NH_3-SCR reaction through the mechanism-enhanced process, Environ. Sci. Technol. 55 (2021) 4017–4026, https://doi.org/10.1021/acs.est.0c08410.

[43] J. Dupin, D. Gonbeau, P. Vinatierb, A. Levasseur, Systematic XPS studies of metal oxides, hydroxides and peroxides, Phys. Chem. Chem. Phys. 2 (2000) 1319–1324, https://doi.org/10.1039/A908800H.

[44] F. Jiang, S. Wang, B. Liu, J. Liu, L. Wang, Y. Xiao, Y. Xu, X. Liu, Insights into the influence of CeO_2 crystal facet on CO_2 hydrogenation to methanol over Pd/CeO_2 catalysts, ACS Catal. 10 (2020) 11493–11509, https://doi.org/10.1021/acscatal.0c03324.

[45] S. Xie, Y. Liu, J. Deng, J. Yang, X. Zhao, Z. Han, K. Zhang, H. Dai, Insights into the active sites of ordered mesoporous cobalt oxide catalysts for the total oxidation of o-xylene, J. Catal. 352 (2017) 282–292, https://doi.org/10.1016/j.jcat.2017.05.016.

[46] M.S. Palmer, M. Neurock, M.M. Olken, Periodic density functional theory study of methane activation over La_2O_3: activity of O_2^-, O^-, O_2^{2-}, oxygen point defect, and Sr^{2+}-doped surface sites, J. Am. Chem. Soc. 124 (2002) 8452–8461, https://doi.org/10.1021/ja0121235.

[47] M. Zhang, H. Gao, J. Chen, E.A. Elimian, H. Jia, Calcination engineering of urchin-like CoO_x-CN catalysts to enhance photothermocatalytic oxidation of toluene via photo-/thermocoupling effect, Appl. Catal. B Environ. 307 (2022) 121208–121219, https://doi.org/10.1016/j.apcatb.2022.121208.

[48] J. Datka, A.M. Turek, J.M. Jehng, I.E. Wachs, Acidic properties of supported niobium oxide catalysts: an infrared spectroscopy investigation, J. Catal. 135 (1992) 186–199, https://doi.org/10.1016/0021-9517(92)90279-q.

[49] Z. Zhang, F. Lin, L. Xiang, H. Yu, Z. Wang, B. Yan, G. Chen, Synergistic effect for simultaneously catalytic ozonation of chlorobenzene and NO over $MnCoO_x$ catalysts: byproducts formation under practical conditions, Chem. Eng. J. 427 (2022) 130929–130943, https://doi.org/10.1016/j.cej.2021.130929.

[50] L. Ding, M. Li, Y. Zhao, H. Zhang, J. Shang, J. Zhong, H. Sheng, C. Chen, J. Zhao, The vital role of surface Brönsted acid/base sites for the photocatalytic formation of free·OH radicals, Appl. Catal. B Environ. 266 (2020) 118634–118641, https://doi.org/10.1016/j.apcatb.2020.118634.

[51] A. Ray. Frost, N. Soisnard, S. Voyer, W. Palmer, Martens, Thermo-Raman spectroscopy of selected layered double hydroxides of formula $Cu_6Al_2(OH)_{16}CO_3$ and $Zn_6Al_2(OH)_{16}CO_3$, J. Raman Spectrosc. 40 (2009) 645–649, https://doi.org/10.1002/jrs.2148.

[52] J. Kloprogge, D. Wharton, L. Hickey, R. Frost, Infrared and Raman study of interlayer anions CO_3^{2-}, NO_3^-, SO_4^{2-} and ClO_4^- in Mg/Alhydrotalcite, Am. Mineral. 87 (2002) 623–629, https://doi.org/10.2138/am-2002-5-604.

[53] C. Schilling, A. Hofmann, C. Hess, M. Ganduglia-Pirovano, Raman spectra of polycrystalline CeO_2: a density functional theory study, J. Phys. Chem. C 121 (2017) 20834–20849, https://doi.org/10.1021/acs.jpcc.7b06643.

[54] E. Conterosito, L. Palin, D. Antonioli, M. Riccardi, E. Boccaleri, M. Aceto, M. Milanesio, V. Gianotti, On the rehydration of organic layered double hydroxides to form low-ordered carbon/LDH nanocomposites, Inorganics 6 (2018) 79–94, https://doi.org/10.3390/inorganics6030079.

[55] J. Zhang, B. Shen, Z. Hu, M. Zhen, S. Guo, F. Dong, Uncovering the synergy between Mn substitution and O vacancy in ZnAl-LDH photocatalyst for efficient toluene removal, Appl. Catal. B Environ. 296 (2021) 120376–120386, https://doi.org/10.1016/j.apcatb.2021.120376.

[56] X. Wang, C. Ma, J. Xiao, Q. Xia, J. Wu, Z. Li, Benzene/toluene/water vapor adsorption and selectivity of novel C-PDA adsorbents with high uptakes of benzene and toluene, Chem. Eng. J. 335 (2018) 970–978, https://doi.org/10.1016/j.cej.2017.10.102.

[57] Y. Li, M. Wei, L. Liu, Q. Xue, B. Yu, Adsorption of toluene on various natural soils: influences of soil properties, mechanisms, and model, Sci. Total Environ. 740 (2020) 140104–140113, https://doi.org/10.1016/j.scitotenv.2020.140104.

[58] X. Zhang, X. Shi, Q. Zhao, Y. Li, J. Wang, Y. Yang, F. Bi, J. Xu, N. Liu, Defects controlled by acid-modulators and water molecules enabled UiO-67 for exceptional toluene uptakes: an experimental and theoretical study, Chem. Eng. J. 427 (2022) 131573–131586, https://doi.org/10.1016/j.cej.2021.131573.

[59] L. Wu, Z. Sun, Y. Zhen, S. Zhu, C. Yang, J. Lu, Y. Tian, D. Zhong, J. Ma, Oxygen vacancy-induced nonradical degradation of organics: critical trigger of oxygen (O_2) in the Fe-Co LDH/peroxymonosulfate system, Environ. Sci. Technol. 55 (2021) 15400–15411, https://doi.org/10.1021/acs.est.1c04600.

[60] F. Zhang, X. Zhu, J. Ding, Z. Qi, M. Wang, S. Sun, J. Bao, C. Gao, Mechanism study of photocatalytic degradation of gaseous toluene on TiO_2 with weak-bond adsorption analysis using in situ far infrared spectroscopy, Catal. Lett. 144 (2014) 995–1000, https://doi.org/10.1007/s10562-014-1213-9.

[61] W. Tan, A. Liu, S. Xie, Y. Yan, T.E. Shaw, Y. Pu, K. Guo, L. Li, S. Yu, F. Gao, F. Liu, L. Dong, Ce-Si mixed oxide: a high sulfur resistant catalyst in the NH_3-SCR reaction through the mechanism-enhanced process, Environ. Sci. Technol. 55 (2021) 4017–4026, https://doi.org/10.1021/acs.est.0c08410.

[62] W. Yang, Y. Peng, Y. Wang, Y. Wang, H. Liu, Za Su, W. Yang, J. Chen, W. Si, J. Li, Controllable redox-induced in-situ growth of MnO_2 over Mn_2O_3 for toluene oxidation: active heterostructure interfaces, Appl. Catal. B Environ. 278 (2020) 119279–119289, https://doi.org/10.1016/j.apcatb.2020.119279.

[63] J. Li, E. Yu, S. Cai, X. Chen, J. Chen, H. Jia, Y. Xu, Noble metal free, CeO_2/$LaMnO_3$ hybrid achieving efficient photo-thermal catalytic decomposition of volatile organic compounds under IR light, Appl. Catal. B Environ. 240 (2019) 141–152, https://doi.org/10.1016/j.apcatb.2018.08.069.

[64] Z. Chen, Y. Peng, J. Chen, C. Wang, H. Yin, H. Wang, C. You, J. Li, Performance and mechanism of photocatalytic toluene degradation and catalyst regeneration by thermal/UV treatment, Environ. Sci. Technol. 54 (2020) 14465–14473, https://doi.org/10.1021/acs.est.0c06048.

[65] Y. Zheng, Y. Su, C. Pang, L. Yang, C. Song, N. Ji, D. Ma, X. Lu, R. Han, Q. Liu, Interface-enhanced oxygen vacancies of CoCuOx catalysts in situ grown on monolithic Cu foam for VOC catalytic oxidation, Environ. Sci. Technol. (2021), https://doi.org/10.1021/acs.est.1c05855.

[66] J. Wu, Y. Cheng, In situ FTIR study of photocatalytic NO reaction on photocatalysts under UV irradiation, J. Catal. 237 (2006) 393–404, https://doi.org/10.1016/j.jcat.2005.11.023.

[67] S. Mo, J. Li, R. Liao, P. Peng, J. Li, J. Wu, M. Fu, L. Liao, T. Shen, Q. Xie, D. Ye, Unraveling the decisive role of surface CeO_2 nanoparticles in the Pt-CeO_2/MnO_2 hetero-catalysts for boosting toluene oxidation: synergistic effect of surface decorated and intrinsic O-vacancies, Chem. Eng. J. 418 (2021) 2408–2439, https://doi.org/10.1016/j.cej.2021.129399.

[68] Z. Sheng, D. Ma, Q. He, K. Wu, L. Yang, Mechanism of photocatalytic toluene oxidation with $ZnWO_4$: a combined experimental and theoretical investigation, Catal. Sci. Technol. 9 (2019) 5692–5697, https://doi.org/10.1039/C9CY01388A.

[69] P. Liu, Y. Liao, J. Li, L. Chen, M. Fu, P. Wu, R. Zhu, X. Liang, T. Wu, D. Ye, Insight into the effect of manganese substitution on mesoporous hollow spinel cobalt oxides for catalytic oxidation of toluene, J. Colloid Interface Sci. 594 (2021) 713–726, https://doi.org/10.1016/j.jcis.2021.03.093.

[70] Y. Li, J. Xue, Q. Shen, S. Jia, Q. Li, Y. Li, X. Liu, H. Jia, Construction of a ternary spatial junction in yolk–shell nanoreactor for efficient photo-thermal catalytic hydrogen generation, Chem. Eng. J. 423 (2021) 130188–130202, https://doi.org/10.1016/j.cej.2021.130188.

[71] J. Li, X. Dong, G. Zhang, W. Cui, W. Cen, Z. Wu, S. Lee, F. Dong, Probing the ring-opening pathways for efficient photocatalytic toluene decomposition, J. Mater. Chem. A 7 (2019) 3366–3374, https://doi.org/10.1039/C8TA11627J.